A Unified Finite Element Approach for Generalized Coupled Thermoelastic Analysis of 3D Beam-Type Structures, Part 2: Numerical Evaluations

M. Filippi
Postdoctoral Research Fellow, e-mail: matteo.filippi@polito.it, Department of Mechanical and Aerospace Engineering, Politecnico di Torino, Corso Duca degli Abruzzi 24, 10129, Torino, Italy,

A. Entezari
PhD Candidate, e-mail: entezari@ae.sharif.edu, Sharif University of Technology, Department of Aerospace Engineering, Azadi Ave, P. O. Box 11155-8639, Tehran, Iran,

E. Carrera
Professor of Aerospace Structures and Aeroelasticity, e-mail: erasmo.carrera@polito.it, Corresponding author, Department of Mechanical and Aerospace Engineering, Politecnico di Torino, Corso Duca degli Abruzzi 24, 10129, Torino, Italy.

Abstract

This paper aims at evaluating the high-fidelity one-dimensional finite elements that have been proposed in the companion paper (Part 1 [1]). Simple structural configurations that are subjected to different loading and boundary conditions have been considered to demonstrate the generality of the proposed approach. Static, quasi-static, and dynamic analyses of the coupled and uncoupled thermoelasticity have been performed. The kinematics of the beam elements have been obtained using bi-dimensional lagrangian expansions with different polynomial orders. In

particular, bi-linear, bi-quadratic, and bi-cubic expansions have been adopted to approximate both displacements and temperature change field. Convergence studies have been carried out by considering finite beam elements with 2, 3, and four nodes. Analytical and numerical solutions have been reported to validate the current results. Besides time histories of displacements and temperature changes, the results have been presented using contour plots in order to highlight the three-dimensional capabilities of the refined beam elements.

Keywords: Coupled Thermoelasticity; Finite Element Method; Carrera Unified Formulation; Lagrange-type expansions.

Introduction

In the companion paper, the Carrera Unified Formulation (CUF) has been used to derive the coupled governing equations according to the classical and generalized theories of thermoelasticity. Even though the beam-like modeling technique has been used, the CUF models provide three-dimensional descriptions of the displacement and temperature fields. Furthermore, the finite element method (FEM) enables complex geometries subjected to arbitrary boundary and loading conditions to be considered. According to the used methodology, the primary variables have been expressed as it follows

$$\begin{aligned} \mathbf{u}(x,y,z,t) &= N_m(y)F_\tau(x,z)\mathbf{U}^{m\tau}(t) \\ T(x,y,z,t) &= N_m(y)F_\tau(x,z)\Theta^{m\tau}(t) \end{aligned} \tag{1}$$

where the subscripts $m\,(m = 1, 2, \cdots, BN)$ and $\tau\,(\tau = 1, 2, \cdots, LN)$ stand for summations. In particular, BN and LN are, respectively, the number of nodes

within each beam element, and the number of terms used to define the approximating theory. The quantities $\mathbf{U}^{m\tau}(t) = \{U_x^{m\tau} \quad U_y^{m\tau} \quad U_z^{m\tau}\}^{\mathrm{T}}$ and $\Theta^{m\tau}(t)$ are the nodal displacements and temperature change at each instant. The terms $N_m(y)$ are the Lagrangian shape functions, while $F_\tau(x, z)$ are functions of the cross-section coordinates. As it is outlined in Part 1 [1], the substitution of Eq. (1) into the equilibrium and energy equations leads to a dynamic system that includes the mass, the damping, and the stiffness matrix, and the loading vector. Within the CUF context, the components of these mathematical operators, which are traditionally called *fundamental nuclei*, consist of integral quantities that are combinations of the $N_m(y)$ and $F_\tau(x, z)$ functions. These expressions are the invariants of the unified formulation, therefore, neither the nature of functions $F_\tau(x, z)$ nor their number LN modifies such mathematical statements. This feature offers, among others, the following advantages with respect to classical finite element approaches

- comparisons between different theories can be easily performed either by enriching the approximating expansions or by changing the functions $F_\tau(x, z)$;
- governing equations are systematically obtained regardless of which theory is considered;
- the modeling anisotropy due to the beam assumption can be overcome with arbitrary refinements of the kinematics expansion;
- the three-dimensional features of the 1D FE-CUF models may significantly facilitate the coupling between computer-aided design and FEM.

This paper has been organized as it follows. Section 2 briefly describes the kinematics adopted and the related assembling procedure, while the numerical

simulations have been presented in Section 3. Eventually, some concluding remarks have been drawn.

Component-wise approach for the coupled thermoelastic problems

In this paper, the approximating expansions have been obtained using bi-dimensional Lagrange functions. The Lagrange-based elements enable the physical surfaces to be modeled adopting arbitrary kinematics. This inherent capability makes it possible to create component-wise (CW) mathematical models, which can accurately describe the geometry of the real structure. Within the CW context, cross sections can be discretized by using different types of triangular and quadrilateral Lagrange elements (LEs) such as linear three-point (denoted as L3), quadratic six-point (L6), bi-linear four-point (L4), bi-quadratic nine-point (L9) and bi-cubic sixteen-point (L16) elements (see Fig. 1).

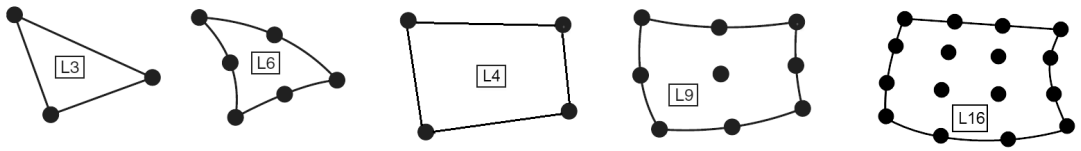

Figure 1: Three-, six-, four-, nine- and sixteen-point (L3, L6, L9 and L16) triangular and quadrilateral Lagrange elements in actual geometry.

Figure 2 shows the distribution of Lagrange points in the actual and natural coordinate systems. In general, the coordinate transformation from an arbitrary cross section referred to (x, z) coordinates to the natural square (ξ, η) is trivial and more details can be found in Ref. [2].

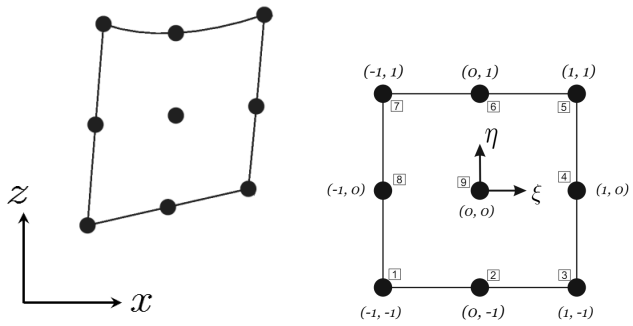

(a) (b)

Figure 2: Sample scheme of L9 element in the actual (a) and the natural (b) coordinate systems.

The Lagrange polynomials for a L4 and a L9 element in the natural coordinate system (ξ, η) are expressed by Eqs. (2) and (3), respectively (see [3])

$$F_\tau(\xi,\eta) = \frac{1}{4}(1+\xi\ \xi_\tau)(1+\eta\ \eta_\tau) \qquad \tau = 1,2,3,4 \tag{2}$$

$$\begin{aligned} F_\tau(\xi,\eta) &= \frac{1}{4}(\xi^2+\xi\ \xi_\tau)(\eta^2+\eta\ \eta_\tau) \qquad \tau = 1,3,5,7 \\ F_\tau(\xi,\eta) &= \frac{1}{2}\eta_\tau^2(\eta^2-\eta\ \eta_\tau)(1-\xi^2) \\ &\quad + \frac{1}{2}\xi_\tau^2(\xi^2-\xi\ \xi_\tau)(1-\eta^2) \qquad \tau = 2,4,6,8 \\ F_\tau(\xi,\eta) &= (1-\xi^2)(1-\eta^2) \qquad \tau = 9 \end{aligned} \tag{3}$$

here $-1 \le \xi \le 1$ and $-1 \le \eta \le 1$, whereas ξ_τ and η_τ are the natural coordinates of τ^{th} Lagrange point of the element. It is observed that the number of functions equals the number of points of the element. Likewise, the 16 polynomials related to a L16 element can be obtained by combining the bi-dimensional functions F_τ^J and F_τ^K as it follows

$$F_\tau^{JK}(\xi,\eta) = F_\tau^J(\xi)F_\tau^K(\eta) \qquad J,K = 1,2,3,4 \qquad \tau = 1,...,16 \tag{4}$$

where the function F_τ^J (or F_τ^K) becomes

$$F_\tau^1(\xi) = \tfrac{1}{16}(\xi - 1)(1 - 9\xi^2) \qquad F_\tau^2(\xi) = \tfrac{9}{16}(1 - \xi^2)(1 - 3\xi)$$
$$F_\tau^3(\xi) = \tfrac{9}{16}(1 - \xi^2)(1 + 3\xi) \qquad F_\tau^4(\xi) = \tfrac{1}{16}(1 + \xi)(9\xi^2 - 1)$$

when J (or K) ranges from 1 to 4.

As far as the longitudinal discretization is concerned, beam elements with two (B2), three (B3) or four (B4) nodes can be chosen. The related shape functions are the 1D Lagrangian polynomials. Figure 3 shows a possible mathematical model used to discretize a simple 3D geometry.

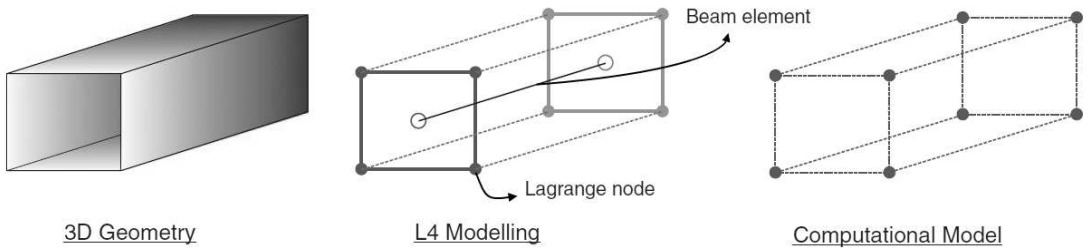

Figure 3: An example of L4 modeling via an L4 element and a linear beam element along the longitudinal axis. 32 total DOF, 16 DOF per beam node, 4 DOF per Lagrange node.

The model consists of one L4 element (1L4) above the cross-section and one linear beam element (1B2) along the longitudinal axis, whose shape functions are N_1 and N_2. The model has 8 Lagrange points that correspond to 32 degrees of freedom (DOF) (4 DOF per each Lagrangian point). The related displacement field and the temperature change are

$$
\begin{aligned}
u_x &= N_m F_\tau U_x^{m\tau} = N_1(F_1 U_x^{11} + \cdots + F_4 U_x^{14}) + N_2(F_1 U_x^{21} + \cdots + F_4 U_x^{24}) \\
u_y &= N_m F_\tau U_y^{m\tau} = N_1(F_1 U_y^{11} + \cdots + F_4 U_y^{14}) + N_2(F_1 U_y^{21} + \cdots + F_4 U_y^{24}) \\
u_z &= N_m F_\tau U_z^{m\tau} = N_1(F_1 U_z^{11} + \cdots + F_4 U_z^{14}) + N_2(F_1 U_z^{21} + \cdots + F_4 U_z^{24}) \\
T &= N_m F_\tau \Theta^{m\tau} = N_1(F_1 \Theta^{11} + \cdots + F_4 \Theta^{14}) + N_2(F_1 \Theta^{21} + \cdots + F_4 \Theta^{24})
\end{aligned}
\tag{5}
$$

For the assembly procedure, Fig. 4 graphically shows the methodology followed to build the CUF matrices. It should be observed that, in this example, the structure has been modeled using two L4 elements above the cross-section, and three 4-node beam elements along the longitudinal axis.

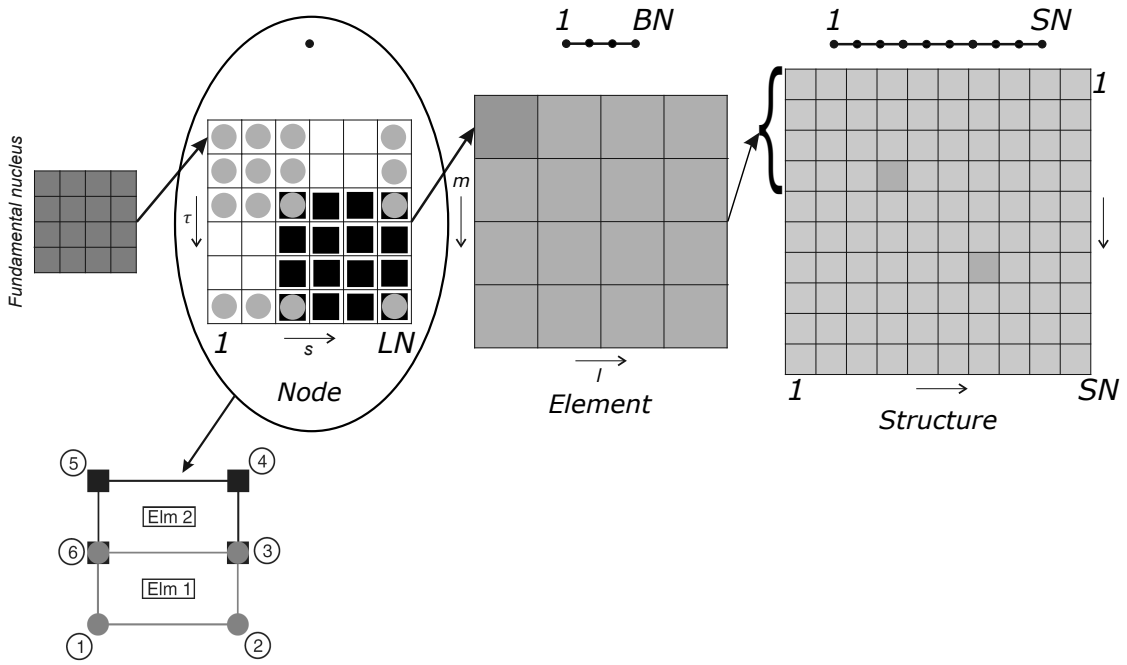

Figure 4: Graphical representation of the assembly procedure. 'LN': Lagrangian points per each beam node; 'BN': number of nodes per each beam element; 'SN': total number of beam nodes.

The total number of DOF of the computational model can be easily computed as

$$\mathrm{DOF} = \sum_{i=1}^{SN} (4 \times LN^{(i)}) \tag{6}$$

where $LN^{(i)}$ and SN represent the number of Lagrangian points of the i-th beam node, and the total number of structural nodes, respectively. According to the example of Fig. 4, Eq. (6) reduces to

$$\mathrm{DOF} = \sum_{i=1}^{10} (4 \times 6) = 240$$

Numerical results

The following section aims at validating the proposed methodology with reference solutions. Firstly, a static coupled thermoelastic analysis has been performed on a simple metallic cantilever beam. The related results, which have obtained with different mathematical models, have been compared with a solution computed with a simple one-dimensional formula. Secondly, the same configuration has been considered for a transient quasi-static analysis.

Finally, the non-dimensional parameters and the consequent expressions of the dimensionless $fundamental\ nuclei$ are presented and the time histories of displacements and temperature change have been computed. To validate the dynamic formulation, the current results have been compared with an analytical and a finite element solution proposed for metallic disks. Eventually, a number of results have been presented by considering beams subjected to different boundary and loading conditions.

Static Coupled Thermoelastic Analysis

The structure is a cantilever square beam, which has been subjected to a heat flux (q=100 W) at the clamped edge. The free tip has been considered at ambient temperature (T_0=20^o C). The cross-section area and the beam length were A = 20 cm^2, and L = 50 cm, respectively. The material is aluminum with the Young's modulus E=73.1 GPa, the Poisson's ratio ν= 0.33, the thermal conductivity κ = 237 W·(m·K)$^{-1}$ and the coefficient of thermal expansion α=23.1×10^{-6} K^{-1}. The analyses have been performed using several mathematical models. In particular, Table 1 lists the temperature changes and the longitudinal displacements along the beam axis using different meshes conceived with 2-node finite elements (B2). Further mesh studies have been performed considering the 4-node beam elements (B4) and different kinematic theories. The results reported in Tabs. 2, 3, and 4 have been obtained using, respectively, a single L4, L9 and L16 element above the cross-section.

It is observed that the predicted temperature changes (T= 105.5 ^{o}C) satisfies the conduction equation

$$q = \kappa\, A\, \frac{T}{L} = 100 \text{ W} \tag{7}$$

For the axial elongations, the CUF results can be compared with a simple one-dimensional relation

$$u_y(y_i) = y_i\, \alpha\, \frac{(T_{y_i} + T_{y_i=0})}{2} \tag{8}$$

where y_i is the axial location. The results revealed that the proposed beam elements ensure a significant rate of convergence. In fact, only 5 elements are enough

Table 1: Displacement and temperature change vs. number of B2 elements, 1L4.

		Location along the y-axis in mm (y_i)					
Nr. elements		0.0	0.1	0.2	0.3	0.4	0.5
5-B2	u_y	0.0	0.319	0.473	0.597	0.670	0.696
	T	105.5	84.38	63.28	42.19	21.09	0.0
10-B2	u_y	0.0	0.263	0.435	0.556	0.629	0.654
	T	105.5	84.38	63.28	42.19	21.09	0.0
20-B2	u_y	0.0	0.245	0.416	0.537	0.611	0.635
	T	105.5	84.38	63.28	42.19	21.09	0.0
30-B2	u_y	0.0	0.240	0.410	0.532	0.605	0.630
	T	105.5	84.38	63.28	42.19	21.09	0.0
50-B2	u_y	0.0	0.236	0.407	0.529	0.602	0.626
	T	105.5	84.38	63.28	42.19	21.09	0.0
100-B2	u_y	0.0	0.235	0.406	0.527	0.601	0.625
	T	105.5	84.38	63.28	42.19	21.09	0.0

Table 2: Displacement and temperature change vs. number of B4 elements, 1L4.

		Location along the y-axis in mm (y_i)					
Nr. elements		0.0	0.1	0.2	0.3	0.4	0.5
5-B4	u_y	0.0	0.242	0.412	0.534	0.607	0.631
	T	105.5	84.38	63.28	42.19	21.09	0.0
10-B4	u_y	0.0	0.236	0.406	0.528	0.601	0.625
	T	105.5	84.38	63.28	42.19	21.09	0.0
20-B4	u_y	0.0	0.234	0.405	0.527	0.600	0.624
	T	105.5	84.38	63.28	42.19	21.09	0.0
30-B4	u_y	0.0	0.234	0.405	0.527	0.600	0.624
	T	105.5	84.38	63.28	42.19	21.09	0.0
50-B4	u_y	0.0	0.234	0.405	0.527	0.600	0.624
	T	105.5	84.38	63.28	42.19	21.09	0.0
100-B4	u_y	0.0	0.234	0.405	0.527	0.600	0.624
	T	105.5	84.38	63.28	42.19	21.09	0.0

Table 3: Displacement and temperature change vs. number of B4 elements, 1L9.

		Location along the y-axis in mm (y_i)					
Nr. elements		0.0	0.1	0.2	0.3	0.4	0.5
5-B4	u_y	0.0	0.242	0.409	0.531	0.604	0.629
	T	105.5	84.38	63.28	42.19	21.09	0.0
10-B4	u_y	0.0	0.233	0.404	0.526	0.601	0.623
	T	105.5	84.38	63.28	42.19	21.09	0.0
20-B4	u_y	0.0	0.232	0.403	0.525	0.599	0.622
	T	105.5	84.38	63.28	42.19	21.09	0.0
30-B4	u_y	0.0	0.232	0.403	0.525	0.598	0.622
	T	105.5	84.38	63.28	42.19	21.09	0.0
50-B4	u_y	0.0	0.232	0.403	0.525	0.598	0.622
	T	105.5	84.38	63.28	42.19	21.09	0.0
100-B4	u_y	0.0	0.232	0.403	0.525	0.598	0.622
	T	105.5	84.38	63.28	42.19	21.09	0.0

Table 4: Displacement and temperature change vs. number of B4 elements, 1L16.

		Location along the y-axis in mm (y_i)					
Nr. elements		0.0	0.1	0.2	0.3	0.4	0.5
5-B4	u_y	0.0	0.242	0.409	0.531	0.604	0.629
	T	105.5	84.38	63.28	42.19	21.09	0.0
10-B4	u_y	0.0	0.233	0.404	0.526	0.598	0.623
	T	105.5	84.38	63.28	42.19	21.09	0.0
20-B4	u_y	0.0	0.231	0.402	0.524	0.597	0.621
	T	105.5	84.38	63.28	42.19	21.09	0.0
100-B4	u_y	0.0	0.231	0.402	0.524	0.597	0.621
	T	105.5	84.38	63.28	42.19	21.09	0.0

to predict the correct values of temperature changes, while models with 10 elements provide converged solutions also for the displacements, regardless of which Lagrange elements are used.

Transient analyses

The dynamic coupled equations derived in Part 1 [1] and reported in Eq. (9) can be solved using different numerical approaches. In this work, the Laplace transform method is adopted for obtaining numerical approximations of the time-dependent solution

$$\mathbf{M}\ddot{\mathbf{\Delta}} + \mathbf{G}\dot{\mathbf{\Delta}} + \mathbf{K}\mathbf{\Delta} = \mathbf{P} \tag{9}$$

Applying the Laplace method, Eq. (9) is transformed in an algebraic system that is function of the Laplace transform parameter $\tilde{s}$

$$(\mathbf{M}\tilde{s}^2 + \mathbf{G}\tilde{s} + \mathbf{K})\mathbf{\Delta}^* = \mathbf{P}^*(\tilde{s}) \tag{10}$$

$\mathbf{\Delta}^*$ and $\mathbf{P}^*$ represent the unknowns and the load vectors in the Laplace domain. Equation (10) can be written as

$$\mathbf{K}_{eq}(\tilde{s})\mathbf{\Delta}^* = \mathbf{P}^*(\tilde{s}) \tag{11}$$

where $\mathbf{K}_{eq}(\tilde{s})$ is the equivalent stiffness matrix that includes inertial, stiffness and damping contributions. The linear system of Eq. (11) is then solved for different values of $\tilde{s}$, and the related results are being expressed in the time-domain using the numerical inversion of Laplace transforms proposed by Durbin [4]. The procedure outlined is used to solve quasi-static as well as dynamic problems according to

which loads are considered.

Quasi-static analysis

The quasi-static response of the previous structure has been analysed. The governing equations have been modified such that the inertial terms, as well as the time variations of strains into the energy equation, are disregarded. The mathematical model used to perform the transient analysis consisted of ten B4 finite elements along the beam axis and one L4 element above the cross-section. The time history of the temperature changes and the longitudinal displacements at different locations along the beam axis are shown in Figs. 5.

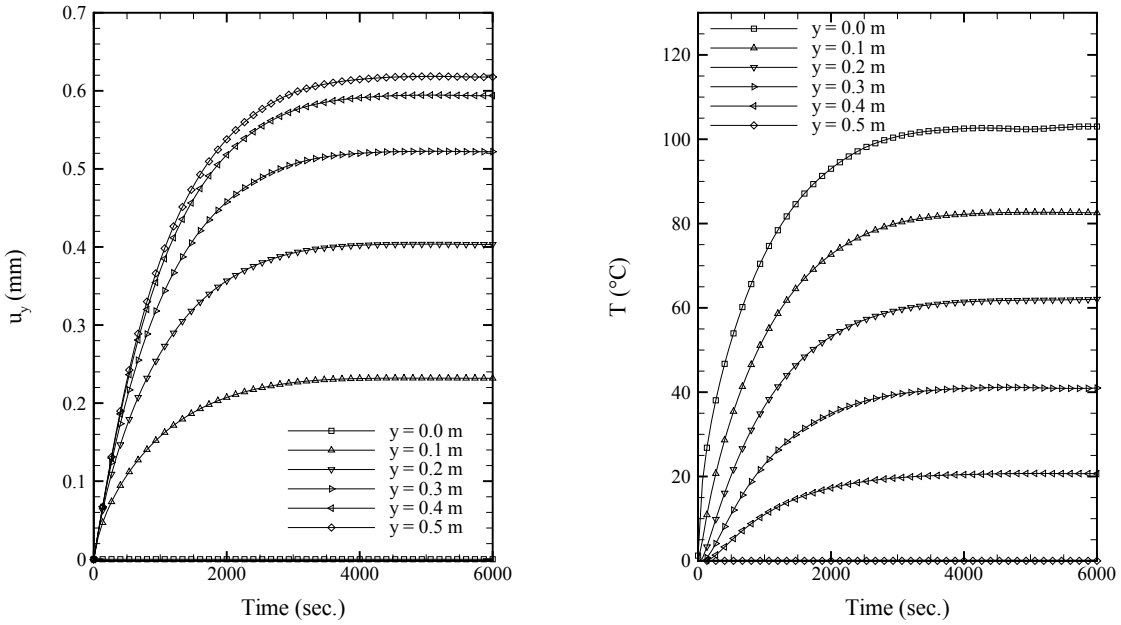

Figure 5: Time histories of axial displacements and temperature changes as functions of the location. 10B4/1L4 model.

The figures show that, as the time passes (time $\rightarrow \infty$), the steady state values of the temperature changes and the axial displacements are reached (see Table 2). In the case in point, the steady-state solutions are obtained after about 2000

seconds. Figures 6 and 7 show the axial displacements and the temperature fields at different times.

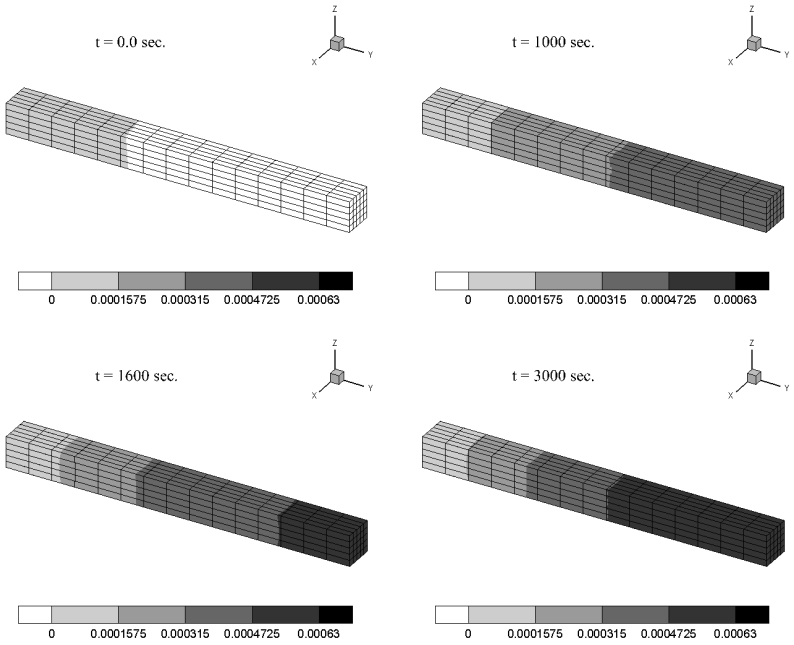

Figure 6: Axial displacements (in meters) at different times. 10B4/1L4 model.

Dynamic analysis

For dynamic problems, it is expedient to express the equations of motion and the energy equation in a dimensionless form. To this end, the following parameters are introduced

$$
\begin{aligned}
&\hat{x}_i = \frac{c\sqrt{\rho(\bar{\lambda}+2\mu)}}{\kappa} x_i \quad ; \quad \hat{t} = \frac{c(\bar{\lambda}+2\mu)}{\kappa} t \quad ; \quad \hat{t}_0 = \frac{c(\lambda+2\mu)}{\kappa} t_0 \\
&\hat{T} = \frac{T}{T_d} \quad ; \quad \hat{u}_i = \frac{c(\lambda+\mu)\sqrt{\rho(\bar{\lambda}+2\mu)}}{\kappa\beta T_d} u_i \\
&\hat{q}_i = \frac{1}{cT_d\sqrt{\rho(\bar{\lambda}+2\mu)}} q_i \quad ; \quad \hat{\sigma}_{ij} = \frac{1}{\beta T_d}\sigma_{ij} \quad ; \quad \hat{t}_i^n = \frac{1}{T_d\beta} t_i^n \\
&\hat{X}_i = \frac{\kappa}{cT_d\bar{\beta}\sqrt{\rho(\bar{\lambda}+2\mu)}} X_i \quad ; \quad \hat{R} = \frac{\kappa}{c^2\rho T_d(\bar{\lambda}+2\mu)} R
\end{aligned}
\tag{12}
$$

where the hat values indicate nondimensional parameters. T_d is a characteristic

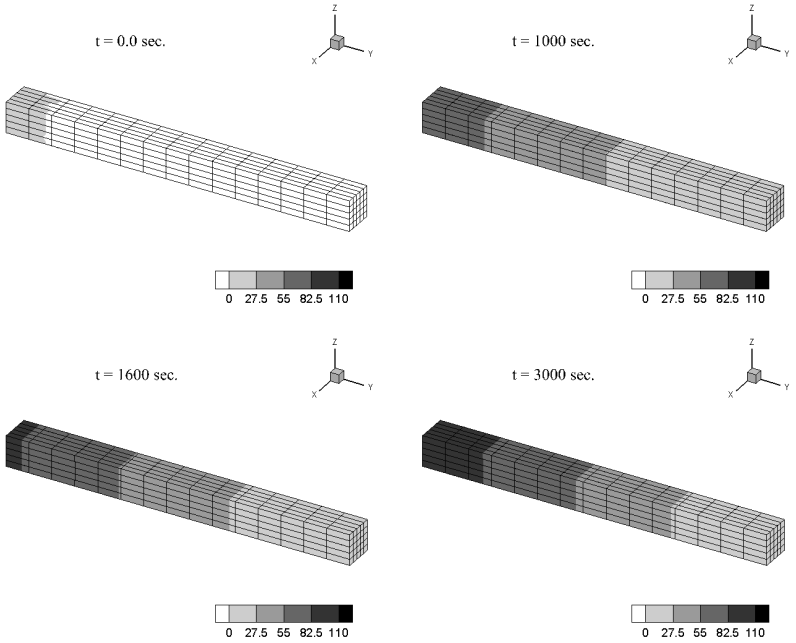

Figure 7: Temperature changes (^{o}C) at different times. 10B4/1L4 model.

temperature and the expressions of $\bar{\lambda}$ and $\bar{\beta}$ may be related to the Lamè constants, λ and μ. Following the procedure outlined in Part 1 [1], the dimensionless governing equations in terms of the fundamental nuclei become

$$[\hat{\mathbf{M}}^{lm\tau s}]\{\hat{\ddot{\boldsymbol{\delta}}}^{m\tau}\} + [\hat{\mathbf{G}}^{lm\tau s}]\{\hat{\dot{\boldsymbol{\delta}}}^{m\tau}\} + [\hat{\mathbf{K}}^{lm\tau s}]\{\hat{\boldsymbol{\delta}}^{m\tau}\} = \{\hat{\mathbf{P}}^{ls}\} \tag{13}$$

where $\{\hat{\boldsymbol{\delta}}^{m\tau}\} = \{\hat{\mathbf{U}}^{ls} \quad \hat{\Theta}^{ls}\}^{\mathrm{T}}$ and $\{\hat{\mathbf{P}}^{ls}\} = \{\hat{\mathbf{F}}^{ls} \quad \hat{Q}^{ls}\}^{\mathrm{T}}$ are the nucleui of the nondimensional unknowns and load vectors, respectively. Using the Laplace transform method, the system (13) reduces to

$$[\hat{\mathbf{K}}_{eq}^{lm\tau s}(\tilde{s})]\{\hat{\boldsymbol{\delta}}^{m\tau^*}\} = \{\hat{\mathbf{P}}^{ls^*}(\tilde{s})\} \tag{14}$$

where $[\hat{\mathbf{K}}_{eq}^{lm\tau s}]$ is the equivalent stiffness matrix that include inertial, stiffness and

damping contributions. Here, the superscript asterisk indicates Laplace transform of the terms.

Neglecting the mechanical damping effect, the explicit expressions of the $[\hat{\mathbf{K}}_{eq}^{lm\tau s}]$ components for isotropic and homogeneous materials based on the Lord-Shulman generalized theory of coupled thermoelasticity can be written as follows

$$
\begin{aligned}
K_{11}^{\tau slm} &= \tilde{s}^2 \left(\triangleleft F_\tau \, F_s \triangleright\right) \mathrm{I}_y^{ml} + \left(\hat{C}_{22} \triangleleft \, F_{\tau,x} \, F_{s,x} \triangleright\right) \mathrm{I}_y^{ml} + \\
&\quad + \left(\hat{C}_{66} \triangleleft \, F_\tau \, F_s \triangleright\right) \mathrm{I}_y^{m,yl,y} + \left(\hat{C}_{44} \triangleleft \, F_{\tau,z} \, F_{s,z} \triangleright\right) \mathrm{I}_y^{ml} \\
K_{12}^{\tau slm} &= \left(\hat{C}_{66} \triangleleft F_\tau \, F_{s,x} \triangleright \right) I_y^{m,yl} + \left(\hat{C}_{23} \triangleleft F_{\tau,x} \, F_s \triangleright \right) I_y^{ml,y} \\
K_{13}^{\tau slm} &= \left(\hat{C}_{44} \triangleleft F_{\tau,z} \, F_{s,x} \triangleright \right) I_y^{ml} + \left(\hat{C}_{21} \triangleleft F_{\tau,x} \, F_{s,z} \triangleright \right) I_y^{ml} \\
K_{14}^{\tau slm} &= -\left(\hat{C}_{\beta} \triangleleft F_{\tau,x} \, F_s \triangleright \right) I_y^{ml} \\
K_{21}^{\tau slm} &= \left(\hat{C}_{66} \triangleleft F_{\tau,x} \, F_s \triangleright \right) I_y^{ml,y} + \left(\hat{C}_{32} \triangleleft F_\tau \, F_{s,x} \triangleright \right) I_y^{m,yl} \\
K_{22}^{\tau slm} &= \tilde{s}^2 \left(\triangleleft F_\tau \, F_s \triangleright \right) I_y^{ml} + \left(\hat{C}_{66} \triangleleft F_{\tau,x} \, F_{s,x} \triangleright \right) I_y^{ml} + \\
&\quad + \left(\hat{C}_{33} \triangleleft F_\tau \, F_s \triangleright \right) I_y^{m,yl,y} + \left(\hat{C}_{55} \triangleleft F_{\tau,z} \, F_{s,z} \triangleright \right) I_y^{ml} \\
K_{23}^{\tau slm} &= \left(\hat{C}_{55} \triangleleft F_{\tau,z} \, F_s \triangleright \right) I_y^{ml,y} + \left(\hat{C}_{31} \triangleleft F_\tau \, F_{s,z} \triangleright \right) I_y^{m,yl} \\
K_{24}^{\tau slm} &= -\left(\hat{C}_{\beta} \triangleleft F_\tau \, F_s \triangleright \right) I_y^{m,yl} \\
K_{31}^{\tau slm} &= \left(\hat{C}_{44} \triangleleft F_{\tau,x} \, F_{s,z} \triangleright \right) I_y^{ml} + \left(\hat{C}_{12} \triangleleft F_{\tau,z} \, F_{s,x} \triangleright \right) I_y^{ml} \\
K_{32}^{\tau slm} &= \left(\hat{C}_{55} \triangleleft F_\tau \, F_{s,z} \triangleright \right) I_y^{m,yl} + \left(\hat{C}_{13} \triangleleft F_{\tau,z} \, F_s \triangleright \right) I_y^{ml,y} \\
K_{33}^{\tau slm} &= \tilde{s}^2 \left(\triangleleft F_\tau \, F_s \triangleright \right) I_y^{ml} + \left(\hat{C}_{44} \triangleleft F_{\tau,x} \, F_{s,x} \triangleright \right) I_y^{ml} + \\
&\quad + \left(\hat{C}_{55} \triangleleft F_\tau \, F_s \triangleright \right) I_y^{m,yl,y} + \left(\hat{C}_{11} \triangleleft F_{\tau,z} \, F_{s,z} \triangleright \right) I_y^{ml} \\
K_{34}^{\tau slm} &= -\left(\hat{C}_{\beta} \triangleleft F_{\tau,z} \, F_s \triangleright \right) I_y^{ml} \\
K_{41}^{\tau slm} &= C \left(\tilde{s}^2 \hat{C}_\beta \hat{t}_0 \triangleleft F_\tau \, F_{s,x} \, \triangleright \, + \tilde{s} \hat{C}_\beta \triangleleft F_\tau \, F_{s,x} \triangleright \right) I_y^{ml} \\
K_{42}^{\tau slm} &= C \left(\tilde{s}^2 \hat{C}_\beta \hat{t}_0 \triangleleft F_\tau \, F_s \, \triangleright \, + \tilde{s} \hat{C}_\beta \triangleleft F_\tau \, F_s \triangleright \right) I_y^{ml,y} \\
K_{43}^{\tau slm} &= C \left(\tilde{s}^2 \hat{C}_\beta \hat{t}_0 \triangleleft F_\tau \, F_{s,z} \, \triangleright \, + \tilde{s} \hat{C}_\beta \triangleleft F_\tau \, F_{s,z} \triangleright \right) I_y^{ml} \\
K_{44}^{\tau slm} &= \left(\tilde{s}^2 \hat{t}_0 \triangleleft F_\tau \, F_s \, \triangleright \, + \tilde{s} \triangleleft F_\tau \, F_s \triangleright \right) I_y^{ml} + \left(\triangleleft F_{\tau,x} \, F_{s,x} \triangleright \right) I_y^{ml} + \\
&\quad + \left(\triangleleft F_\tau \, F_s \triangleright \right) I_y^{m,yl,y} + \left(\triangleleft F_{\tau,z} \, F_{s,z} \triangleright \right) I_y^{ml}
\end{aligned}
$$

where

$$\lhd \cdots \rhd = \int_{A^{(e)}} \ldots dA$$

$$\left(I_y^{ml},\, I_y^{m,yl},\, I_y^{ml,y},\, I_y^{m,yl,y}\right) = \int_{L^{(e)}} \left(N_m N_l,\, N_{m,_y} N_l,\, N_m N_{l,_y},\, N_{m,_y} N_{l,_y}\right) dy$$

and the elastic dimensionless coefficients are

$$\begin{aligned}
\hat{C}_\beta &= \frac{\beta}{\bar{\beta}} \\
\hat{C}_{11} = \hat{C}_{22} = \hat{C}_{23} &= \frac{(\lambda + 2\mu)}{(\bar{\lambda} + 2\mu)} \\
\hat{C}_{44} = \hat{C}_{55} = \hat{C}_{66} &= \frac{\mu}{(\bar{\lambda} + 2\mu)} \\
\hat{C}_{12} = \hat{C}_{13} = \hat{C}_{23} &= \frac{\lambda}{(\bar{\lambda} + 2\mu)}
\end{aligned}$$

while the coupling parameter is defined as

$$C = \frac{T_0 \bar{\beta}^2}{c\rho(\bar{\lambda} + 2\mu)}$$

Likewise, by considering surface and volume forces, the general expression of the loading vector in the Laplace domain becomes

$$\{\hat{\mathbf{P}}^{ls}\} = \left\{ \begin{array}{c} \int\limits_{S^{(e)}} \hat{t}_x^{n*} F_s \, N_l dS + \int\limits_{V^{(e)}} \hat{X}_x^* F_s \, N_l dV \\ \int\limits_{S^{(e)}} \hat{t}_y^{n*} F_s \, N_l dS + \int\limits_{V^{(e)}} \hat{X}_y^* F_s \, N_l dV \\ \int\limits_{S^{(e)}} \hat{t}_z^{n*} F_s \, N_l dS + \int\limits_{V^{(e)}} \hat{X}_z^* F_s \, N_l dV \\ \int\limits_{V^{(e)}} [(\hat{t}_0 s + 1)\hat{R}^*] F_s \, N_l dV - \int\limits_{S^{(e)}} (\hat{q}_{input}^*) F_s \, N_l dS \end{array} \right\} \tag{15}$$

To investigate the accuracy of the presented formulation, an example is chosen from [5] where the coupled thermoelasticity of a disk is analyzed using the axisymmetric finite element method. An exact solution for this problem was also presented by Kouchakzadeh and Entezari [6]. Both approaches were derived using the plane stress assumption. According to this hypothesis, the dimensionless parameters of Eq. (12) have been computed by imposing that $\bar{\lambda} = \frac{2\mu}{\lambda+2\mu}\lambda$ and $\bar{\beta} = \frac{2\mu}{\lambda+2\mu}(3\lambda+2\mu)\alpha$. The dimensionless inner and outer radii of the disk are assumed to be 1 and 2, respectively. While the outside boundary is traction free with zero temperature change, the inner boundary is radially fixed and exposed to a step function heat flux that is defined as the Heaviside unit step function. Thus, the loading vector (see Eq. (15)) reduces to

$$\{\hat{\mathbf{P}}^{ls}\} = \left\{ 0 \quad 0 \quad 0 \quad - \int\limits_{S^{(e)}} (F_s \, N_l / \tilde{s}) dS \right\}^{\mathrm{T}} \tag{16}$$

The numerical value of the coupling parameter is assumed to be 0.02. The material of the disk is aluminum with Lamè constants $\lambda = 40.4$ GPa, $\mu = 27$ GPa, and $\alpha = 23 \times 10^{-6}$ K^{-1}, $\rho = 2707$ kg·m^{-3}, $\kappa = 204$ W·m^{-1}. The disk has been modeled using one 3-node beam element along the longitudinal axis, and 5×20 L9 elements along the radial and circumferential directions, respectively. The time histories of

the dimensionless temperature change and radial displacement computed at the mid-radius based on the classical coupled thermoelasticity are shown in Figs. 8 and 9.

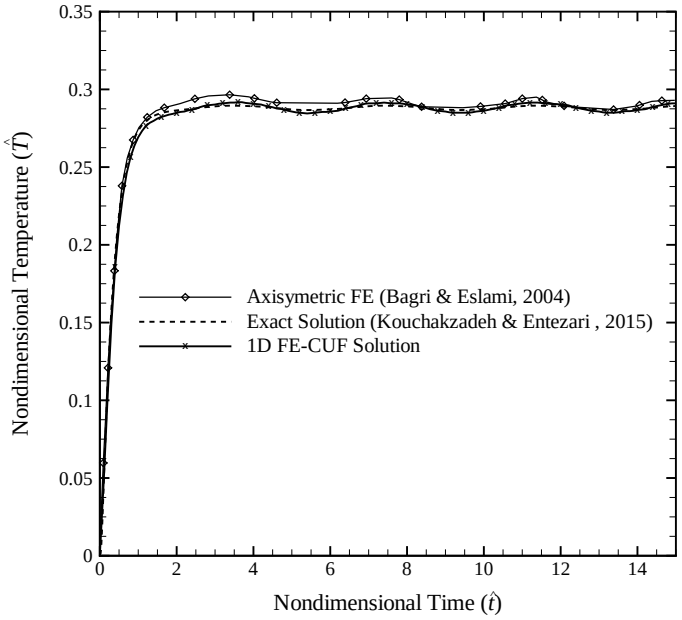

Figure 8: Time history of the temperature change at the mid-radius.

The comparisons revealed that the 1D FE-CUF solution has been able to reproduce the analytical results in terms of both displacement and temperature change. Slight differences can be observed between the axisymmetric solution proposed by Bagri and Eslami [5] and the other approaches.

The classical coupled thermoelastic responses of isotropic and prismatic beams have been here considered. The three-dimensional governing equations have been solved in the dimensionless form with $\bar{\lambda} = \lambda$, and $\bar{\beta} = \beta$. In the first numerical application, the edge of the square cross-section has a dimensionless length equal to $\hat{l}_b = 0.05$, while the beam length is assumed to be $\hat{L}_b = 0.5$. The material is the same of the previous example. The dimensionless temperature change at the

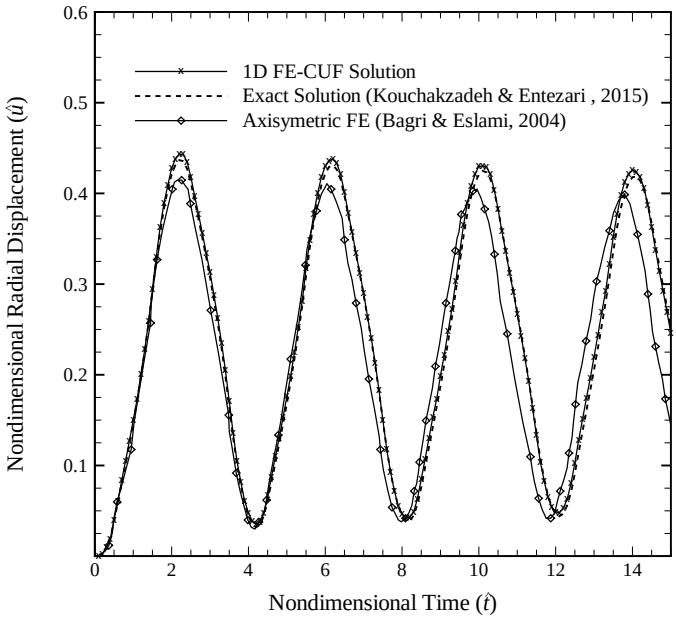

Figure 9: Time history of the radial displacement at the mid-radius.

top surface has been defined as $\hat{T}(\hat{x},\, \hat{y},\, \hat{z} = 0.025, \hat{t}) = 1 - e^{-\hat{t}}$ while the bottom surface has been considered thermally isolated. The simply-supported mechanical boundary conditions have been simulated by preventing only the transverse displacement at both ends ($\hat{u}_z = 0$). Ten 4-node beam elements have been used to discretize the structure along the longitudinal direction, while different two-dimensional meshes have been adopted to model the cross-section. Figures 10 and 11 shows the time histories of the transverse nondimensional displacement and the temperature change computed with the bi-linear, the bi-quadratic, and the bi-cubic Lagrange elements. The reported results have been taken in the mid-point of the beam ($\hat{x} = \hat{l}_b/2$, $\hat{y} = \hat{L}_b/2$, $\hat{z} = \hat{l}_b/2$). It is observed that all mathematical models provided the same time history for the temperature change. On the other hand, the L4 element is not a convergent solution since it has predicted larger transverse displacements and an higher oscillating frequency than the refined meshes. For

the case in point, the L9 model represents the best trade-off between accuracy and computational cost.

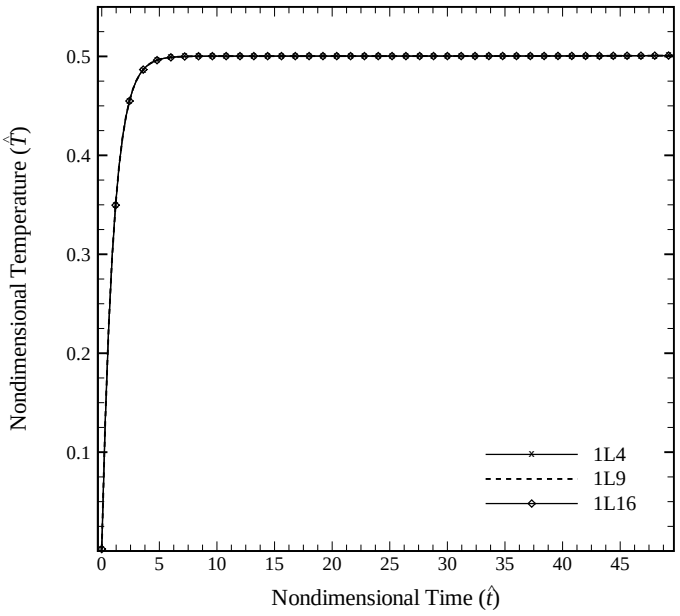

Figure 10: Time history of the temperature change at the mid-point. $T_0 = 293$ K, relaxation time $\hat{t}_0 = 0$.

Figure 12 shows the deformed configurations of the beam due to the dimensionless temperature fields at different times. It can be observed that the maximum transverse displacement is reached at about $\hat{t} = 7.8$.

The same structure has been then considered cantilever with the clamped end subjected to the temperature change $\hat{T}(\hat{x},\, \hat{y} = 0,\, \hat{z}, \hat{t}) = 1 - e^{-100\hat{t}}$. The used mathematical model consisted of 1 L9 above the cross-section and 10 4-node beam elements along the y-axis. The analyses have been carried out according to the classical and the generalized thermoelastic theories. For the LS approach, the dimensionless relaxation time has been assumed equal to $\hat{t}_0$ =0.64.

The time histories of the temperature change and the axial displacement com-

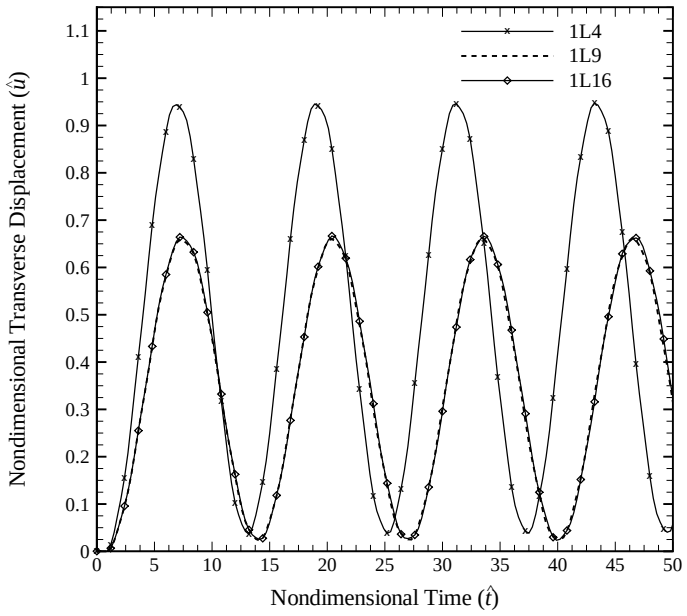

Figure 11: Time history of the transverse displacement at the mid-point. $T_0 = 293$ K, relaxation time $\hat{t}_0 = 0$.

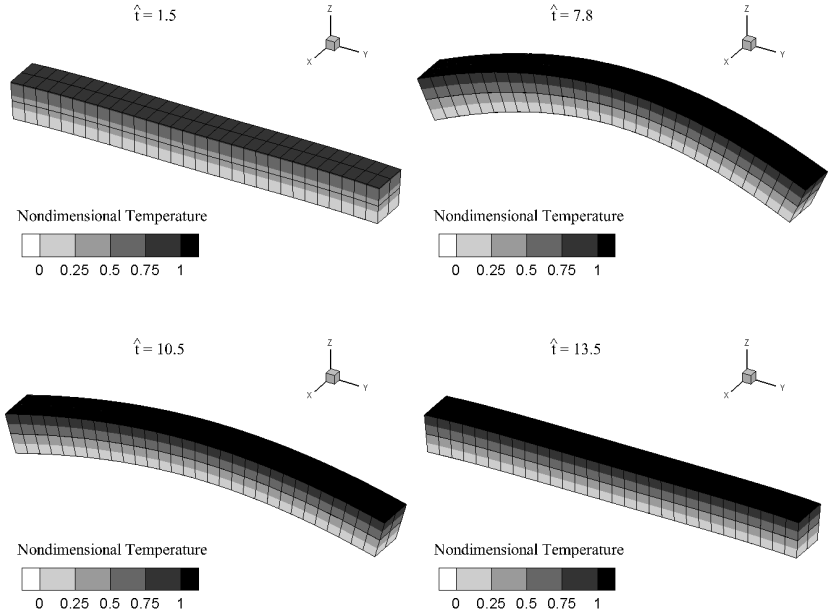

Figure 12: Deformed configurations and nondimensional temperature change distributions at different nondimensional times. 10B4/1L9 model.

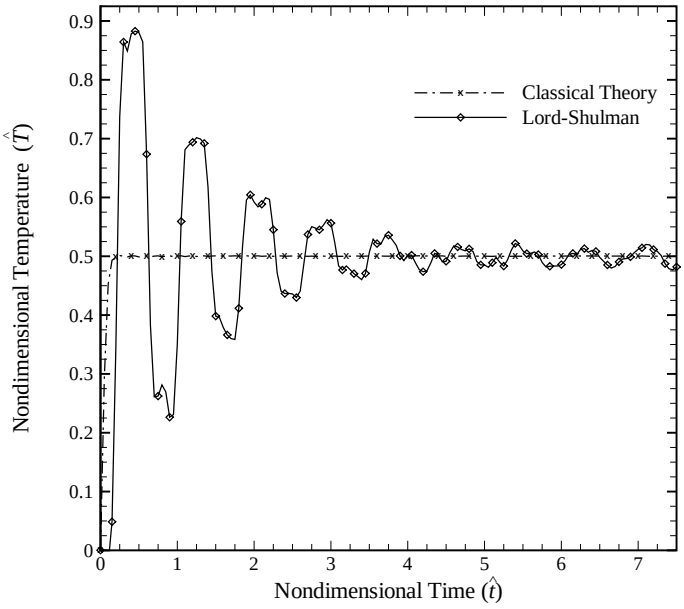

Figure 13: Time history of the temperature change at the mid-point. $T_0 = 293$ K.

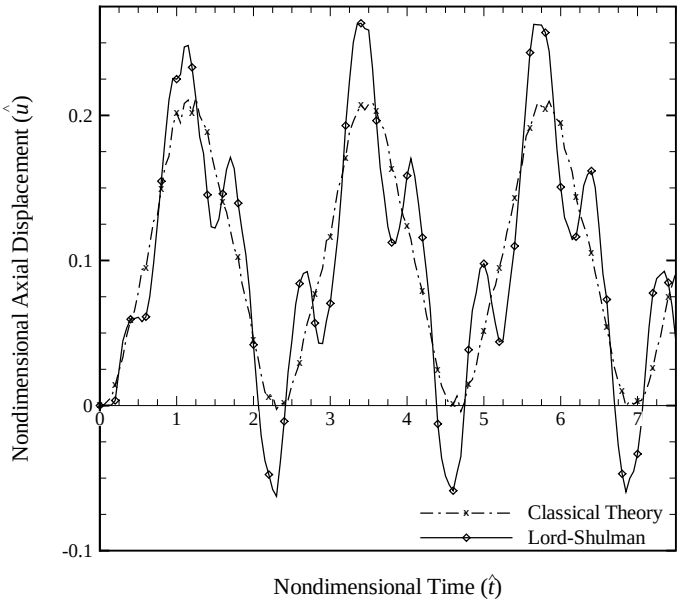

Figure 14: Time history of the transverse displacement at the mid-point. $T_0 = 293$ K.

puted in the mid-point are shown in Figs. 13 and 14, respectively. Contrary to what predicted by the classical thermoelastic theory, the temperature significantly oscillates before to reach the steady state value when the Lord-Shulman model is adopted. Moreover, from Fig. 14, it should be observed that the classical approach underestimated the displacement amplitude with respect to the LS theory. The generalized theory detected some peaks of the temperature and displacement within the considered time interval.

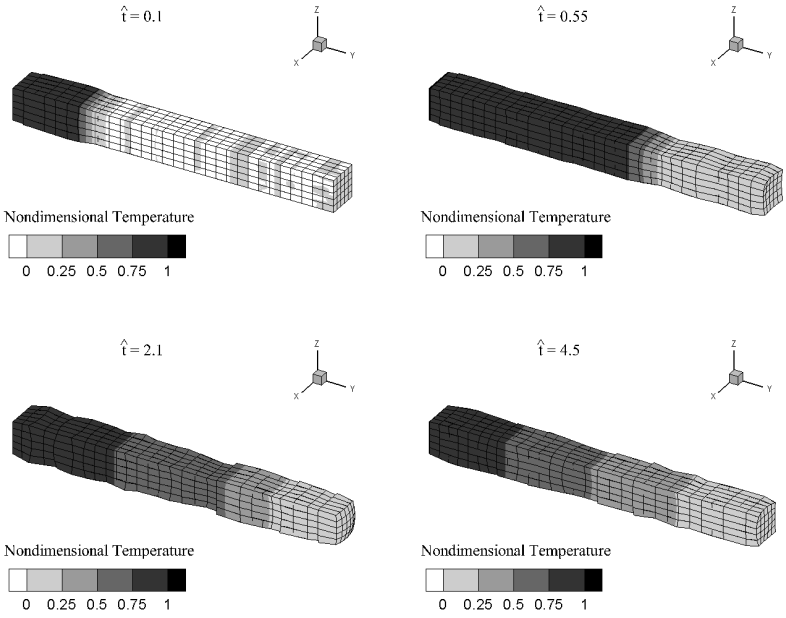

Figure 15: Deformed configurations and nondimensional temperature change distributions at different nondimensional times. Lord-Shulman theory. 10B4/1L9 model.

The deformed configurations of the beam have been shown in Fig. 15 together with the temperature changes at different instants. The three-dimensional capabilities of the CUF beam elements make it possible to detect, besides the axial displacement, the cross-sectional deformations.

Conclusion

The capabilities of high-fidelity beam formulations have been evaluated in the study of coupled thermoelastic responses. One-dimensional finite elements have been developed using the Carrera Unified Formulation. The primary variables, namely the three displacements and the temperature changes, have been approximated using Lagrange-type expansions. The system of equations has been obtained according to classical and generalized theories of thermoelasticity. The proposed approach has been validated through comparisons with available reference solutions considering static, quasi-static, and dynamic analyses. Simulations have been performed on isotropic and homogeneous structures. As expected, the accuracy given by the 1D CUF elements is extremely subordinate to the order of the Lagrange-type expansions. Significant differences between the results obtained by bi-linear and higher-order elements have been observed in some cases. It is noteworthy that the L9 and L16 elements provided accurate solutions with excellent rates of convergence. The CUF formalism enables one to obtain three-dimensional descriptions of the displacement and temperature changes fields with an acceptable computational cost.

Reference

[1] A. Entezari, M. Filippi, and E. Carrera, A Unified Finite Element Approach for 3D Generalized Coupled Thermoelastic Analysis, Part 1: Equations and Formulation (under review), *Journal of Thermal Stresses*, 2017.

[2] K. Bathe, *Finite Element Procedures*, Prentice-Hall International Series in, Prentice Hall, 1996.

[3] E. Carrera and M. Petrolo, Refined One-Dimensional Formulations for Laminated Structure Analysis, *AIAA journal*, vol. 50, pp. 176–189, 2012.

[4] F. Durbin, Numerical inversion of Laplace transforms: an efficient improvement to Dubner and Abate's method, *The Computer Journal*, vol. 17, pp. 371–376, 1974.

[5] A. Bagri and M. Eslami, Generalized coupled thermoelasticity of disks based on the Lord–Shulman model, *Journal of Thermal Stresses*, vol. 27, pp. 691–704, 2004.

[6] M. A. Kouchakzadeh and A. Entezari, Analytical solution of classic coupled thermoelasticity problem in a rotating disk, *Journal of Thermal Stresses*, vol. 38, pp. 1267–1289, 2015.